

Gao, Z., Yang, J., Li, G., Ferber, T., Feng, J., Li, Y., Fu, H., Jaegermann, W., Monroe, C. W. and Huang, Y. (2022) TiO₂ as second phase in Na₃Zr₂Si₂PO₁₂ to suppress dendrite growth in sodium metal solid-state batteries. *Advanced Energy Materials*, 12(9), 2103607.

There may be differences between this version and the published version. You are advised to consult the publisher's version if you wish to cite from it.

This is the peer reviewed version of the following article:

Gao, Z., Yang, J., Li, G., Ferber, T., Feng, J., Li, Y., Fu, H., Jaegermann, W., Monroe, C. W. and Huang, Y. (2022) TiO₂ as second phase in Na₃Zr₂Si₂PO₁₂ to suppress dendrite growth in sodium metal solid-state batteries. *Advanced Energy Materials*, 12(9), 2103607, which has been published in final form at <http://dx.doi.org/10.1002/aenm.202103607>

This article may be used for non-commercial purposes in accordance with [Wiley Terms and Conditions for Self-Archiving](#).

<http://eprints.gla.ac.uk/265508/>

Deposited on: 14 March 2022

TiO₂ as second phase in Na₃Zr₂Si₂PO₁₂ to suppress dendrite growth in sodium metal solid-state batteries

Zhonghui Gao^{1,#}, Jiayi Yang^{2,#}, Guanchen Li^{3,4}, Thimo Ferber⁵, Junrun, Feng⁶, Yuyu, Li⁷, Haoyu Fu¹, Wolfram Jaegermann⁵, Charles W. Monroe^{3,4}, Yunhui Huang^{2,*}

¹*School of Materials Science and Engineering, Tongji University, Shanghai 201804, China.*

²*School of Materials Science and Engineering, Huazhong University of Science and Technology, Wuhan, Hubei 430074, China.*

³*Department of Engineering Science, University of Oxford, Parks Road, OX1 3PJ, UK.*

⁴*The Faraday Institution, Harwell Campus, Didcot, OX11 0RA, UK.*

⁵*Technische Universität Darmstadt, Materials Science Department, Surface Science Division, Jovanka-Bontschits-Str. 2, 64287 Darmstadt, Germany.*

⁶*Department of Chemical Engineering, University College London, Roberts Building, Torrington Place, London WC1E 7JE, UK.*

⁷*Key Laboratory of Optoelectronic Chemical Materials and Devices of Ministry of Education, Jiangnan University, Wuhan, 430056, China.*

(#) These authors contribute equally to this work.

Abstract

Solid-state sodium-metal batteries will not achieve reasonable power density without electrolytes that solve the dendrite (filamentation) problem. Metal-filament formation during plating at ceramic/metal interfaces can cause electrical failure by internal short-circuit or mechanical failure by electrolyte fracture. Herein, we present a $\text{Na}_3\text{Zr}_2\text{Si}_2\text{PO}_{12}$ (NZSP) sodium-ion-conducting NASICON electrolyte in which TiO_2 is incorporated as an additive, leading to a two-phase composite NZSP(TiO_2) with improved density, Young's modulus, hardness, grain structure, and bulk permittivity. These features of NZSP(TiO_2) suppress dendrite growth along grain boundaries, microcracks, and micropores. As well as demonstrating ultralow ceramic/Na kinetic resistance with electrochemical measurements, we perform X-ray photoelectron spectroscopy probe interfacial reaction mechanisms. The TiO_2 phase forms within grain boundaries and along NZSP surfaces. This modifies the two-phase material's microstructure and improves its electrochemical performance, while also increasing the critical current density for dendrite formation. We discuss design guidelines to mitigate microscopic defects and dendrites in two-phase ceramic electrolytes.

1. Introduction

Solid-state batteries composed of ceramic-oxide electrolytes and alkali-metal anodes have the potential to deliver safer batteries with higher specific energy than traditional liquid-electrolyte Li-ion or Na-ion batteries ^[1-3]. Na₃Zr₂Si₂PO₁₂ (NZSP)-based NASICON materials with competitive ionic conductivity that also have high chemical and electrochemical stability are being investigated as electrolytes for solid-state batteries with metallic Na electrodes ^[4-6]. It is theoretically predicted that the NASICON materials can prevent Na dendrite formation due to their high shear modulus ^[7]. However, when the NZSP-based solid-state electrolyte (SSE) is used in combination with metallic Na, it always suffers from failure due to the penetration through the SSE of Na dendrites, which propagate during the plating process.

The main factors that make ceramic SSEs susceptible to growth of alkali-metal dendrites are grain boundaries and microscopic defects in the bulk SSE, as well as contact loss at the SSE/metal interface ^[8-11]. According to the model proposed by Monroe and Newman ^[12], if the shear modulus of a SSE is more than twice that of metallic Li, the SSE/Li interface should in principle be morphologically stable, thereby suppressing dendrite initiation arising from the nonuniform current associated with surface roughness on the micrometer scale. Most state-of-the-art inorganic SSEs are synthesized by conventional solid-state sintering methods, which form polycrystalline materials containing numerous pores and grain boundaries, however. These are the main pathways along which dendrites grow in today's SSEs, and were not considered by Monroe and Newman ^[13-15]. For example, the lithium-ion conductive oxide garnet Li₇La₃Zr₂O₁₂ is susceptible to metallic-Li dendrite penetration through interconnected pores and grain boundaries ^[7]. In this case, grain boundaries and the surfaces of interconnected pores may provide enough electron conductivity to support Li filament propagation by direct plating within the material. Alternatively, electronic conductivity of SSEs arising from atomic defects can promote the deposition of metal inside the bulk SSE ^[16]. Development of SSEs with high density and low electronic conductivity is needed to suppress dendrite growth.

The dynamic change of the SSE/metal interfacial resistance during cycling owes in part to the deterioration of physical contact^[17, 18]. Void formation during stripping leads to an uneven electric-field distribution at the interface, which strongly affects subsequent metal plating. The voids form and accumulate when cation flux through the electrolyte side of the interface exceeds the maximum rate at which metal atoms can diffuse or creep toward the interface on the metal side^[19, 20]. Since cation flux relates to local current density, poor interfacial contact exacerbates void formation, a feedback mechanism that causes voids to accumulate during cycling. Once the local current density in areas of SSE/metal contact exceeds the so-called ‘critical current density’, metal-dendrite growth will occur^[21].

Some strategies concentrated on interface modification have been developed to address voiding and critical currents. Artificial solid-electrolyte interphase (SEI) layers have been introduced to reduce interfacial resistance and suppress metal dendrite growth^[22, 23]. Various coatings have been applied to improve wettability and/or chemical stability between the electrolyte and electrode. Films that have been used to improve wettability of Li or Na and suppress Li/Na dendrites include simple oxides like Al₂O₃^[24] and TiO₂^[25], metal layers such as Au^[26] and Mg^[27], and non-metallic Si^[28] and Ge^[29] films. Although artificial SEIs have been shown to improve wettability and increase the critical current density, they have not yet attained improvements that prevent dendrites eliminated at the higher cycling currents demanded for power applications. Furthermore, tailored SEI films at SSE/metal interfaces may not be mechanically stable upon cycling. If SEI layers are poorly ion conducting and brittle, they may crack during cycling, introducing domains of very high current density that can exacerbate filamentation^[30-33].

Targeting improved bulk properties of ceramic electrolytes is a simpler path to dendrite mitigation. For ceramic electrolytes, it has been found that alkali-metal dendrite initiation and cycle life both correlate with density and mechanical properties, grain shape and size, concentration of microscopic defects, bulk permittivity, and metal-wetting energetics^[34, 35]. In this work, we show that TiO₂ can be used as an

additive to ceramic $\text{Na}_3\text{Zr}_2\text{Si}_2\text{PO}_{12}$ that tunes the above-mentioned properties, producing a composite material that suppresses Na dendrites during cycling. We explore the effects of TiO_2 on the phase composition, microstructure, mechanical properties, and ionic/electronic conductivity of NZSP. The inclusion of TiO_2 as second phase in NZSP to fill grain boundaries and coat particle surfaces not only inhibits formation of Na dendrites, raising the critical current density in symmetric Na/NZSP(TiO_2)/Na cells, but also improves the wetting of NZSP(TiO_2) by metallic Na. We further show extraordinary electrochemical performance of cells that use the two-phase electrolyte against a $\text{Na}_3\text{V}_2(\text{PO}_4)_3$ (NVP) cathode. We discuss how both the extraordinary electrochemical performance of NVP/NZSP(TiO_2)/Na cells and the higher critical current density can be attributed to changes in microstructure and physicochemical properties incurred by the presence of TiO_2 .

2. Results and discussion

Figure 1 shows scanning-electron micrographs of the cross-section and surface microstructures NZSP and NZSP(TiO_2) alongside energy-dispersive X-ray spectroscopy (EDS) data to show how various elements are distributed in the composite. Dense microstructure and consistent grains are critical both for the transport of Na^+ ions and for dendrite suppression ^[36]. Figures 1b and 1c show that NZSP with an average grain size of 1.4 μm exhibits a porous microstructure, both on the surface and in a material cross-section. The average pore size of the NZSP sample is 3.2 μm , as shown in Figure S1. In contrast, NZSP containing 2 wt% TiO_2 shows much denser morphology and significantly reduced porosity, as can be seen in Figure 1f. The pellet of NZSP(TiO_2) had a smaller total volume than the NZSP pellet (Figure S2), which demonstrates the improvement of the NZSP(TiO_2). Figures 1g and 1h show that the NZSP(TiO_2) pellet has a uniform and dense morphology, with an average grain size of 1.9 μm . The grain-size distribution of NZSP(TiO_2) and a best-fit with a normal distribution are provided in Figure S3. It appears that the TiO_2 additive promotes more intimate contact of NZSP grains, hence decreasing interconnected porosity and improving grain-boundary microstructure. Moreover, TiO_2 additive can

decreased the sintering temperature, thus inhibited the grain growth and made a homogenous size distribution, which is beneficial for the densification process of NZSP. The high relative density achieved in the NZSP(TiO_2) pellets likely eliminates porosity as a variable in the following analyses of mechanical properties and electrochemical response.

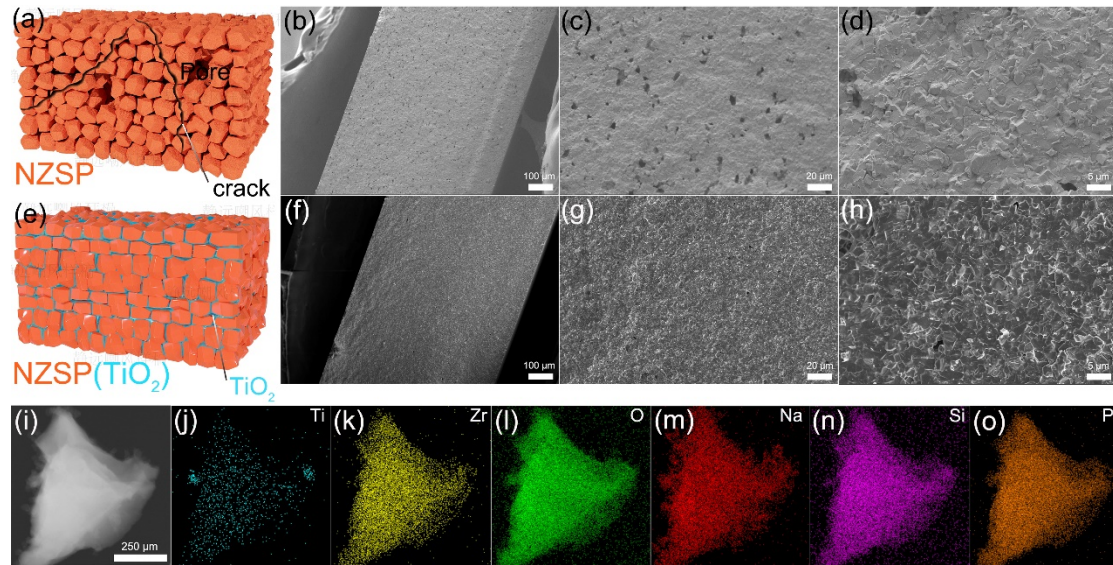


Figure 1. SEM images of surface and cross-sectional microstructures of the as-prepared NZSP and NZSP(TiO_2) pellets. (a) Schematic structure of the NZSP, NZSP with cracks and pores synthesized by the conventional solid-state sintering method. (b) SEM image for cross-section of the NZSP pellet. (c-d) top-view SEM images of a polished NZSP pellet, showing fairly large pores. (e) Schematic structure of the NZSP(TiO_2) material, with the second TiO_2 phase distributed at NZSP grain boundaries and particle surfaces. (f) SEM images within a cross section and (g-h) at the of a polished NZSP(TiO_2) pellet, showing almost no porosity. (i) Transmission electron microscopy image and (j-o) EDS elemental mappings of Ti, Zr, O, Na, Si and P in a NZSP(TiO_2) particle.

Local elemental mappings around a NZSP(TiO_2) particle show an overall homogeneous distribution of the elements Ti, Zr, O, Na, Si and P, as shown in Figure 1i-1o. The elemental mappings of NZSP for comparison are shown in Figure S4 and

Table S2. In addition to the usually employed elemental mapping analysis for single particles of NZSP(TiO₂), we performed time-of-flight secondary ion mass spectrometry (ToF-SIMS) to obtain further information about the grain composition and TiO₂ distribution within the NZSP(TiO₂) ceramic. As shown in Figures S5 and S6, the intensity distribution of the secondary-ion fragment of interest, TiO₂⁺, is very uniform for NZSP(TiO₂) (the analysis areas were 50 × 50 μm² and 300 × 300 μm²). The Ti appears to be relatively evenly distributed throughout the material.

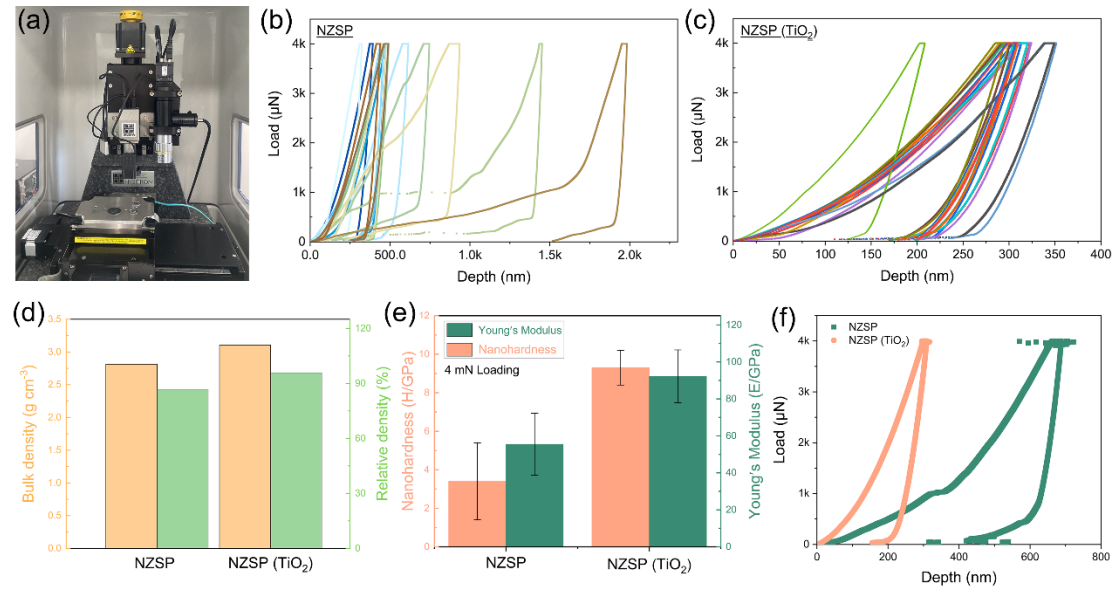


Figure 2. Mechanical properties for NZSP and NZSP(TiO₂) pellets. (a) Digital photo of the nanoindentation apparatus. (b-c) Loading-unloading curves obtained by nanoindentation tests for 15 randomly selected points on the NZSP and NZSP(TiO₂) pellets, demonstrating uniformity of the mechanical-strength distribution. (d) Bulk density and relative density of the NZSP and NZSP(TiO₂). (e) Nanoindentation results for hardness and Young's modulus. (f) Average force/displacement responses up to 4000 μN for NZSP and NZSP(TiO₂).

In general, ceramic SSEs have some pre-existing defects and are prone to crack if metal ions insert into such defects and grain boundaries [37,38]. Thus, the mechanical strength of an SSE is expected to influence its susceptibility to dendrite formation and growth. Nanoindentation measurements were therefore performed to assess the

mechanical response of NZSP and NZSP(TiO₂). Mechanical properties were examined with the nanoindenter shown in Figure 2a. At least 15 indentations were performed for each pellet. Load/displacement curves for NZSP and NZSP(TiO₂) are shown in Figures 2b and Figure 2c, respectively. The distribution of mechanical strength across the NZSP(TiO₂) surface is more uniform than NZSP. Addition of TiO₂ increases the bulk density of NZSP dramatically, from 2.8 to 3.1 g cm⁻³. Porosity is correspondingly lower; the relative density increases from 86.7% to 95.9%, as shown in Figure 2d. Compared with NZSP, both hardness (*H*) and Young's modulus are obviously improved in NZSP(TiO₂) (Figure 2e): the values of *E* and *H* for NZSP are 55.5 ± 16.8 GPa and 3.4 ± 2 GPa, respectively, whereas those for NZSP(TiO₂) are respectively 92.2 ± 14.3 GPa and 9.3 ± 0.9 GPa. Figure 2f shows typical indentation load-displacement curves for NZSP and NZSP(TiO₂). The large difference in strength between NZSP and NZSP(TiO₂) suggest that strength correlates strongly with the density of and interconnection within the microstructure.

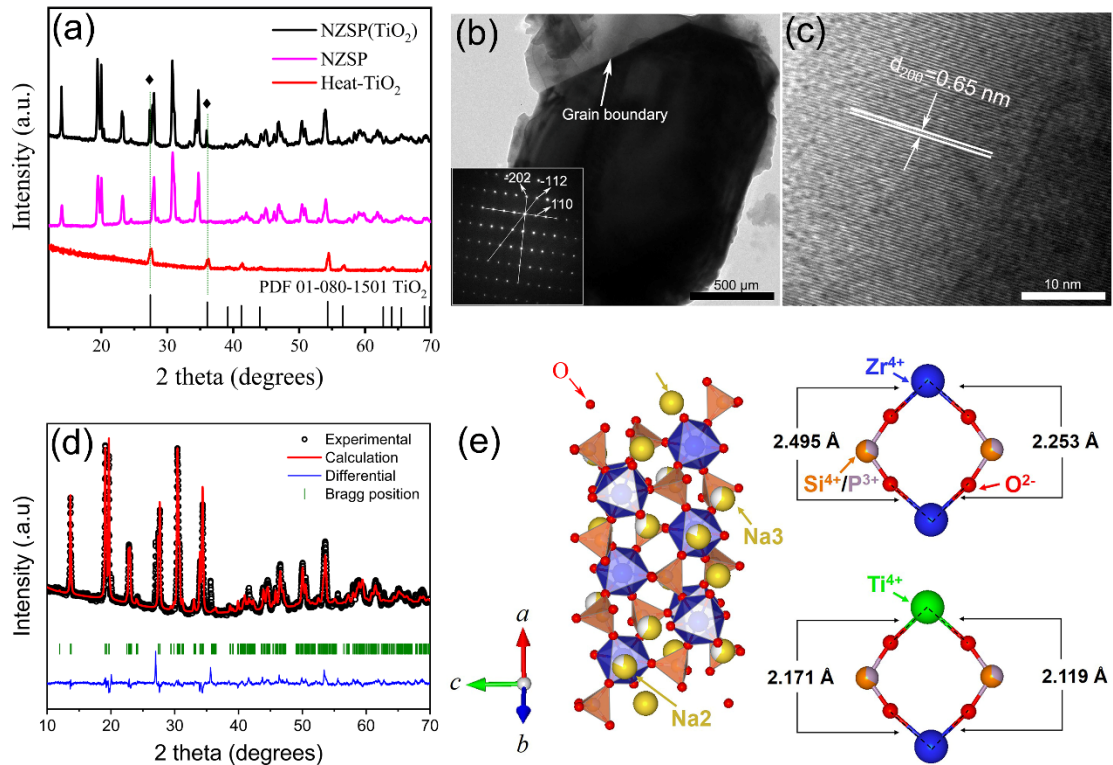


Figure 3. Structural characterization of NZSP(TiO₂). (a) Comparison of diffraction patterns of as-prepared NZSP and NZSP(TiO₂). (b) Transmission electron microscopy

image of as-prepared NZSP(TiO₂) particle, with inset selected-area diffraction pattern. (c) High-resolution transmission electron micrograph of NZSP(TiO₂), in the region indicated by the red rectangle in (b). (d) Rietveld refinement of the powder diffraction pattern for NZSP(TiO₂). (e) The crystal structure, Ti-O, and Zr-O bond length in NZSP(TiO₂). The red, yellow, green, blue and light orange balls in Figure 3e correspond to the O, Na, Ti, Zr and Si atoms in NZSP(TiO₂) structure, respectively.

X-ray diffraction patterns from the NZSP and NZSP(TiO₂) materials are compared in Figure 3a. The NZSP sample shows high purity; all the diffraction peaks can be indexed to a monoclinic structure (PDF 01-084-1200) with a space group of *C2/c*. TiO₂ is detected in NZSP(TiO₂) sample and the diffraction peaks identify with pure TiO₂ (PDF 01-080-1501), demonstrating that TiO₂ exists as a second phase within the NZSP(TiO₂) composite. Figure 3b and the selective area electron diffraction in the inset show the single-crystal nature of a NZSP(TiO₂) particle peeled from the ceramic pellet. Figure 3c gives a high-resolution transmission electron microscopy image of NZSP(TiO₂), showing an interplanar spacing of 0.65 nm, corresponding to the (200) planes of NZSP. Compared with the pure NZSP crystal structure in Figure S7, no obvious difference is detected. Rietveld refinement result of the NZSP(TiO₂) diffraction pattern suggests that some Ti atoms occupy sites originally occupied by Zr in the NZSP lattice, as shown in Figure 3d. Since the radius of Ti⁴⁺ (0.68 Å) is smaller than that of Zr⁴⁺ (0.72 Å), substituting Zr⁴⁺ with Ti⁴⁺ decreases the lattice parameters. The crystal parameters for NZSP(TiO₂) are $a = 15.6683$, $b = 9.0681$, and $c = 9.2401$, while those for NZSP are $a = 15.7614$, $b = 9.1218$, and $c = 9.2951$. If the added Ti ions were fully incorporated into the NZSP lattice, it would be expected to displace 10% of the Zr in NZSP, but the observed occupancy of Ti in the NZSP lattice is only about 2%. Thus, most of the TiO₂ additive appears to contribute to the second phase, expected to be distributed at grain boundaries and on the surface [39].

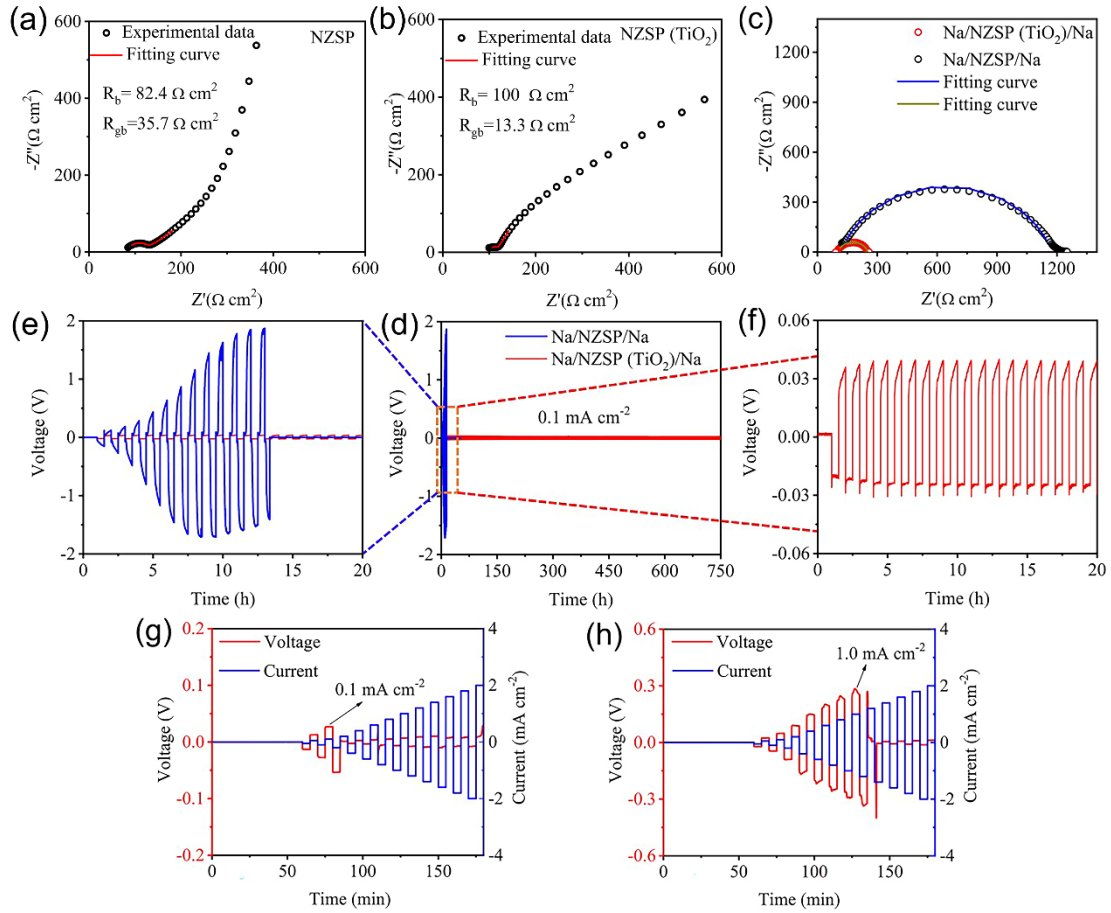


Figure 4. Electrochemical behaviour of NZSP(TiO₂) at 25 °C. Impedance spectra and fits for (a) Au/NZSP/Au and (b) Au/NZSP(TiO₂)/Au cells. (c) Impedance spectra and fits for Na/NZSP/Na and Na/NZSP(TiO₂)/Na cells. (d) Voltage response in symmetric Na/electrolyte/Na cells during galvanostatic cycling at $\pm 0.1 \text{ mA cm}^{-2}$. Details of the area marked by the dashed orange box are shown in (e) and (f). (g-h) Critical current measurement: galvanostatic cycling at current densities stepping from 0.05-2 mA cm^{-2} at 25 °C for (g) NZSP and (h) NZSP(TiO₂).

The distributed TiO₂ second phase within NZSP appears to homogenize grain size and significantly increase the compact contact of NZSP grains, which may encourage higher Na⁺ mobility. Ionic conductivities of NZSP and NZSP(TiO₂) between Au blocking electrodes were measured by electrochemical impedance spectroscopy at 25 °C. Figure 4a and 4b show Nyquist plots for NZSP and

NZSP(TiO₂), respectively. The semicircle at moderate frequencies (100 Hz-10 kHz) is associated with the total resistance of the bulk and grain boundaries of the NZSP, and the low-frequency tail arises from the interfacial capacitance at the Na-ion blocking Au electrodes. Bulk ionic conductivity mainly depends on the grain resistance (R_b) and grain-boundary resistance (R_{gb}). According to fitting calculation with an equivalent-circuit model (Figure S8 and Table S3), the Na-ion conductivity at 25 °C is $6.1 \times 10^{-1} \text{ mS cm}^{-1}$ for NZSP and $6.6 \times 10^{-1} \text{ mS cm}^{-1}$ for NZSP(TiO₂). The R_{gb} value of NZSP is $35.7 \text{ } \Omega \text{ cm}^2$ and that of NZSP(TiO₂) is $13.3 \text{ } \Omega \text{ cm}^2$. The decrease in R_{gb} for NZSP(TiO₂) presumably owes to densification of the microstructure and promotion of grain connection by the added TiO₂, which would be expected to encourage Na transport. The electronic conductivity of NZSP was found to be $4.9 \times 10^{-9} \text{ S cm}^{-1}$ and that of NZSP(TiO₂) was $4.3 \times 10^{-9} \text{ S cm}^{-1}$, as shown in Figure S9. Thus, the TiO₂ additive neither decreased Na mobility nor increased electronic conductivity.

Electrochemical stability and critical current density were evaluated in Na/NZSP/Na and Na/NZSP(TiO₂)/Na symmetric cells by both impedance spectroscopy and galvanostatic cycling. As shown in Figure 4c, two distinct arcs appear in the Nyquist plots for symmetric Na/electrolyte/Na cells. Figure S10 displays how impedance spectra of Na/NZSP/Na and Na/NZSP(TiO₂)/Na symmetric cells were fitted with equivalent circuits. The interfacial contact resistances of $R_{\text{Na/NZSP}}$ and $R_{\text{Na/NZSP(TiO}_2\text{)}}$ are 1060 and 149 $\Omega \text{ cm}^2$, respectively (Table S4), demonstrating that the TiO₂ additive significantly decreases interfacial resistance. This improvement can be mainly attributed to more conformal interfacial contact, arising from better wettability between metallic Na and NZSP(TiO₂). Previous studies by the authors have confirmed the observation that TiO₂ improves the wettability of NZSP/Na interfaces [25].

Na plating and stripping experiments were carried out to evaluate the interfacial resistance and cycling behavior of the Na/NZSP(TiO₂) interface. When cycled at 0.1 mA cm⁻², the Na/NZSP(TiO₂)/Na cell immediately achieves a stable voltage response with an amplitude of $33 \pm 3 \text{ mV}$. The system cycles for 750 h without any signs of

performance degradation, indicating that Na dendrite formation has been effectively suppressed, as shown in Figure 4d. In contrast, the Na/NZSP/Na symmetric cell exhibits a steadily increasing voltage polarization, and short-circuits after 14 h, at which time the polarization is 1.8 V (Figure 4e). Thus, it can be concluded that 0.1 mA cm⁻² is above the critical current density for NZSP, but below the critical current density for the two-phase NZSP(TiO₂) composite.

To more finely resolve the critical currents, symmetrical Na/NZSP(TiO₂)/Na cells were constructed and subjected to stripping and plating at steadily increasing current densities. As shown in Figure 4g, the pure NZSP electrolyte fails after the current density increases above 0.1 mA cm⁻², in line with the observation in cycling experiments. For NZSP(TiO₂), the cell does not short circuit until a current of 1 mA cm⁻² is reached (Figure 4h) an order of magnitude higher.

Li and Monroe proposed a formula ^[40], validated by experiments ^[41], which predicts quantitatively how critical current is expected to vary with properties including SSE/metal interfacial impedance, as well as the bulk permittivity and grain size of the SSE. The higher critical current density of the NZSP(TiO₂)/Na interface can be attributed to its lower interfacial resistance, as well as the higher density and more adherent grain structure of NZSP(TiO₂). According to Li and Monroe, the critical current density i_c of a polycrystalline SSE is influenced by its grain surface-to-volume ratio α_v and a surface-energy difference $\Delta\gamma$,

$$i_c = \frac{\sqrt{6\varepsilon|\alpha_v\Delta\gamma|}}{R_{\text{int}}C_{\text{int}}} \quad (1)$$

where R_{int} and C_{int} are the areal interfacial resistance and specific capacitance, respectively. Since C_{int} and the dielectric permittivity ε of NZSP are expected to be similar to those of NZSP(TiO₂), the higher critical current density for the composite material can be attributed in part to lower interfacial resistance. Note from Figure 4c, however, that the interfacial resistance of NZSP(TiO₂)/Na is only about a factor of 4 lower than NZSP/Na, whereas the critical current density is about 10 times higher.

Thus, the stress associated with grain adhesion that blocks intragranular Na plating, $\alpha_V \Delta \gamma$, must be substantially larger (around six times higher) within NZSP(TiO₂). This is in line with the substantially improved wettability provided by TiO₂.

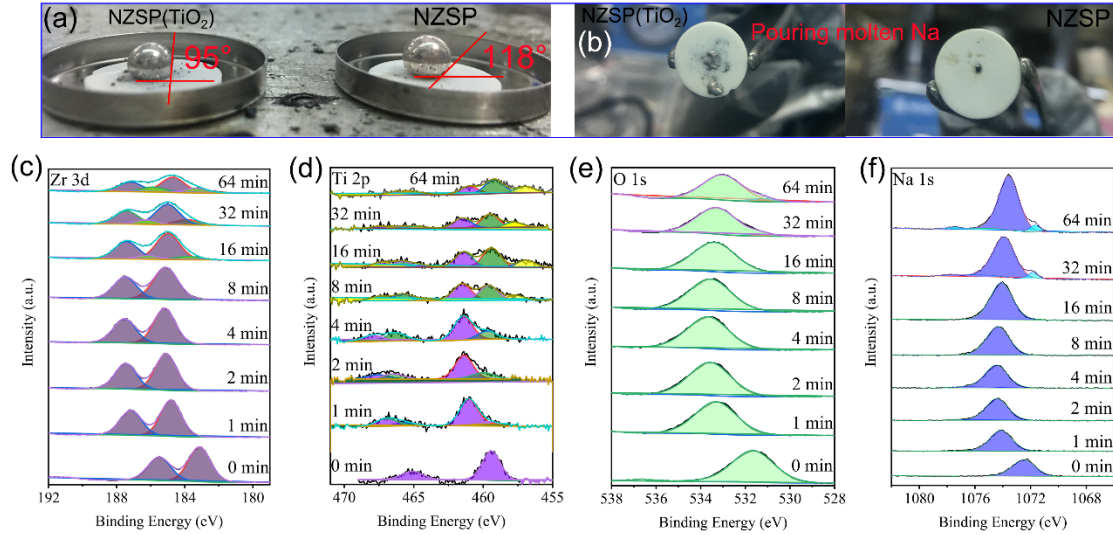


Figure 5. Characterization of NZSP/Na and NZSP(TiO₂)/Na interfacial properties. (a) Contact angle measurement for molten metallic Na on NZSP and NZSP(TiO₂) surfaces, demonstrating improved wetting of the composite by Na. (b) Photographs providing qualitative confirmation of better Na adhesion: after pouring off the surface molten Na, metallic Na prefers to adhere to NZSP(TiO₂) surface. X-ray photoemission spectra of (c) Zr 3d, (d) Ti 2p, (e) O 1s, and (f) Na 1s regions for the stepwise deposition of the metallic Na on the NZSP(TiO₂) surface, showing their evolution with increasing Na deposition time.

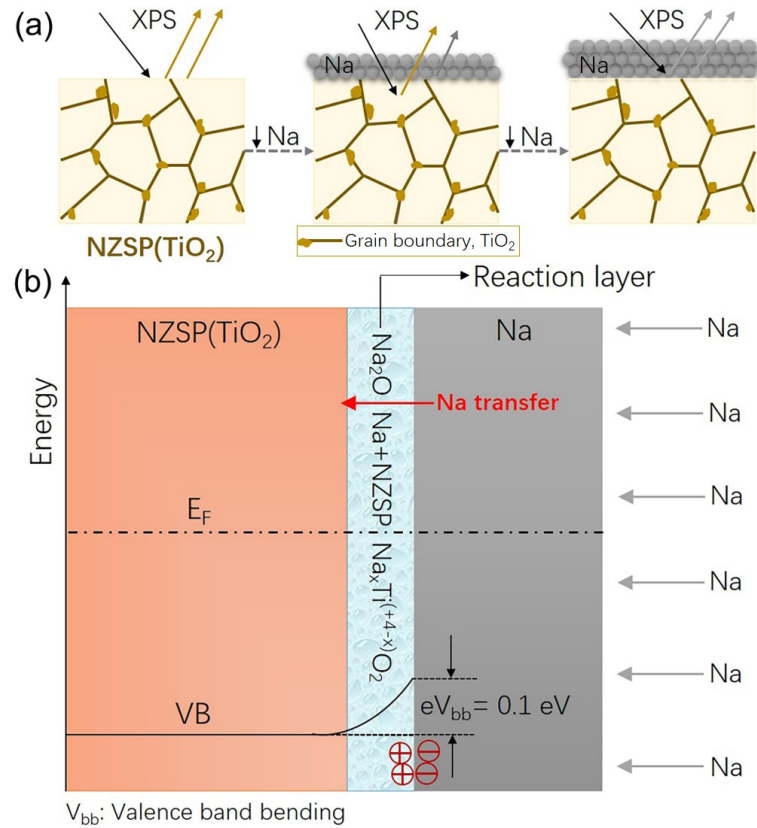


Figure 6. NZSP(TiO₂)/Na interface analysis based on X-ray photoemission spectroscopy (XPS). (a) Schematic diagram of the NZSP(TiO₂)/Na interface tested with subsequent deposition and X-ray analytical steps. (b) Illustration of energy-level alignment at the NZSP(TiO₂)/Na interface deduced from XPS.

It has been confirmed that the wettability of NZSP by metallic Na influences the interface contact and interface resistance. Figure 5b qualitatively confirms better wettability, showing that small droplets of molten Na spread out on and adhere more to the NZSP(TiO₂) surface. More quantitative information is provided by contact-angle measurements, performed with molten Na on heated electrolyte surfaces. As shown in Figure 5a, the as-prepared pure NZSP exhibits a much higher contact angle (118°) than that of NZSP(TiO₂) (95°). According to the above-evaluated contact angle θ , W_{ad} for NZSP/Na and NZSP(TiO₂)/Na interfaces can be calculated by using the Young-Dupré equation^[41]: $W_{ad} = \sigma_{Na} (1 + \cos \theta)$ ($\sigma_{Na} = 0.2523 \text{ J m}^{-2}$). The W_{ad} value of Na/NZSP(TiO₂) (0.23 J m⁻²) is higher than that of Na/NZSP (0.13 J m⁻²).

Moreover, comparison of the contact-angle measurements from Figure 5a using Young's equation shows that $\sec(118^\circ)/\sec(95^\circ) = 5.7$, showing that the difference in surface energies coincides almost exactly with the observed difference in critical current densities between NZSP and NZSP(TiO₂).

A surface science approach based on XPS was employed to detect the real contact properties between NZSP(TiO₂) with metallic Na. Surface impurities were removed by thermal treatment at 450 °C in Ar and O₂. After thermal treatment, the intensity of the C 1s peak (Figure S11) decreases significantly. In Figures S12 and S13, the spectra of Si 2p and P 2p core levels obtained by the Na deposition experiments show no obvious core-level shifts. Figures 5c-5f show the Zr 3d, Ti 2p, O 1s, and Na 1s core-level spectra during deposition of Na at a Na/NZSP(TiO₂) interface. Changes in the NZSP(TiO₂) correlate strongly with the amount of Na deposited, indicative of reactions occurring at the Na/NZSP(TiO₂) interface. A tiny amount of Zr³⁺ is detected as shown in Figure 5c. The Ti⁴⁺ in NZSP(TiO₂) gradually reduces to Ti³⁺ and Ti²⁺ after >2 min of metallic Na deposition. Na intercalation apparently induces the reduction of Ti⁴⁺O₂ and forms an interphase of Na_xTiO₂. In the O 1s region, the bulk NZSP(TiO₂) main peak has a binding energy of 533.4 eV; a slight shoulder at lower binding energies of 531.2 eV can be attributed to Na₂O. After Na deposition onto the surface for 32 min, a metallic Na peak is detected from the typical Na 1s spectrum at 1074.1 eV, which demonstrates that Na deposition does not cause continuous reduction of Zr⁴⁺ and Ti⁴⁺, an observation that holds for deposition times ranging from 16 to 64 min. All the studied elements in Figure 5e-5f show an initial shift to higher binding energies upon contact with metallic Na, which we attribute to a Fermi-level shift up in the near-surface region due to Na intercalation [42, 43]. This shift relaxes and decreases with additional deposition of Na, presumably because of Na diffusion into the bulk of the NZSP(TiO₂). We also observe the formation of reaction products upon Na deposition and a coordinated shift to lower binding energies. The binding energy shift of Ti⁴⁺ (2.3 eV) is not identical with the valence band maximum of 2 eV (Figure S14), presumably owing to uptake of sodium

in NZSP(TiO₂). In summary, it can be concluded that interphases of Na₂O and Na_xTiO₂ form, which further improve contact between NZSP(TiO₂) and Na. Figure 6a shows schematic diagrams illustrating the proposed mechanism of interfacial evolution during stepwise deposition of metallic Na.

It is also noteworthy that a band bending upwards (binding energies shifted to lower values) was observed for the following deposition steps of metallic Na, which can be attributed to formation of a space-charge layer near the interface (Figure 6b). Both chemically distinct interphases and space charging at the NZSP(TiO₂)/Na interface can promote contact and passivate further side reactions between NZSP(TiO₂) with Na metal.

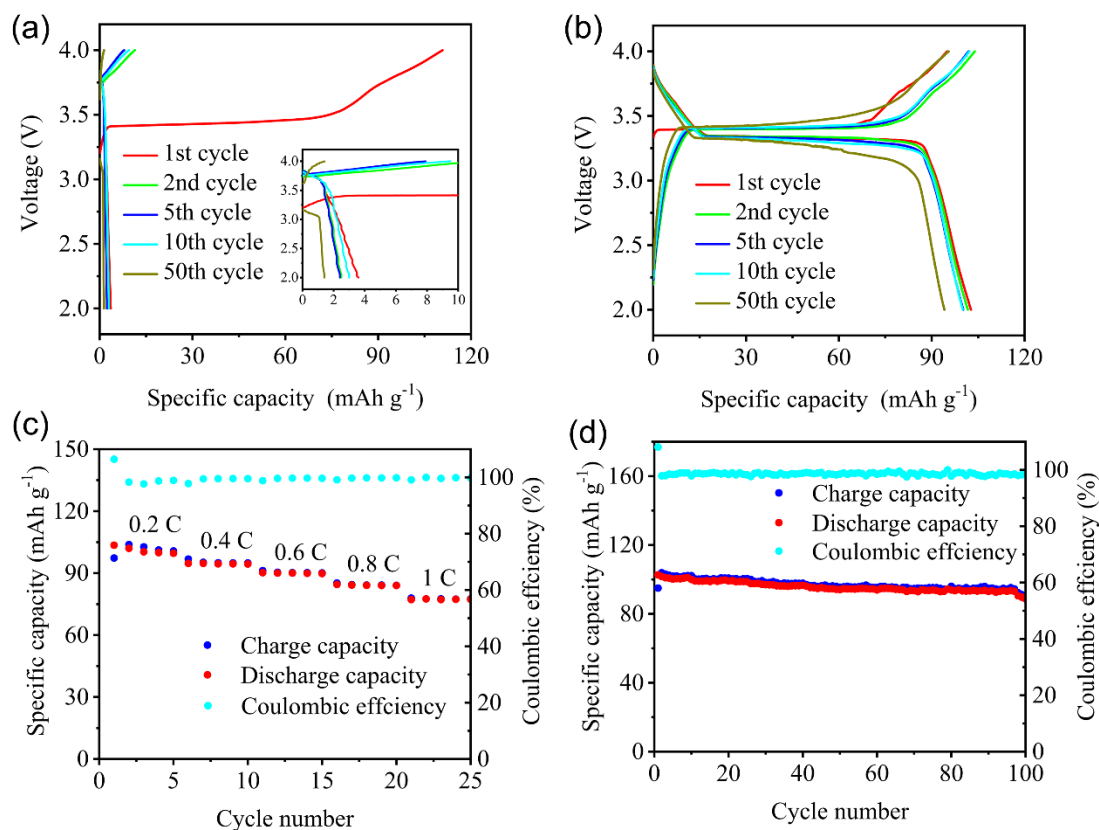


Figure 7. Electrochemical characterization of a solid-state battery composed of a Na₃V₂(PO₄)₃ cathode, NZSP(TiO₂) SSE, and Na-metal anode. (a-b) Charge/discharge curves with NZSP and NZSP(TiO₂) at the 1st, 2nd, 5th, 10th, and 50th cycles, respectively. Note that 5 mL of liquid organic electrolyte (1 M NaClO₄ in EC:DMC,

1:1 by neat precursor volume) was added to each cell to wet the cathode/electrolyte interface. (c) Rate performance of the $\text{Na}_3\text{V}_2(\text{PO}_4)_3/\text{NZSP}(\text{TiO}_2)/\text{Na}$ cell. (d) Cycle performance of a $\text{Na}_3\text{V}_2(\text{PO}_4)_3/\text{NZSP}(\text{TiO}_2)/\text{Na}$ full cell at 0.2 C.

The full cell adopts $\text{NZSP}(\text{TiO}_2)$, a Na metal anode, and a carbon coated $\text{Na}_3\text{V}_2(\text{PO}_4)_3/\text{super P/PVDF}$ composite cathode (abbreviated NVP). Figure 7a and 7b show the charge-discharge voltage curves of the cell (NZSP) for different cycles (1st, 2nd, 5th, 10th, and 50th) at 0.2 C (1C = 117 mAh g⁻¹). The $\text{NZSP}(\text{TiO}_2)$ cell delivers a discharge capacity of 102.8 mAh g⁻¹ at 1st cycle and 94.1 mAh g⁻¹ at 50th cycle at 0.2 C. Classic plateaus at 3.4 V during charge and at 3.3 V during discharge validate that the $\text{NZSP}(\text{TiO}_2)$ cell has low overpotential (~0.1 V). By contrast, the NZSP cell shows asymmetric charge and discharge performance and it works not well. Figure 7c shows charge/discharge profiles for $\text{NZSP}(\text{TiO}_2)$ cells at various rates from 0.2 C up to 1 C at 25 °C. The $\text{NZSP}(\text{TiO}_2)$ cell delivers discharge capacities of 94.7, 84.5, 77.3 and 49.5 mAh g⁻¹ at rates of 0.4, 0.6, 0.8 and 1 C, respectively, much higher than those of NZSP cell. In Figure 7d, the discharge capacity of the $\text{NZSP}(\text{TiO}_2)$ cell slowly decays from 102.8 to 88.7 mAh g⁻¹ within 100 cycles at 0.2 C, indicating enhanced cycling stability in comparison to the NZSP cell.

Conclusion

Reducing porosity and microscopic defects of NZSP with additives, as well as altering its grain structure, is an effective strategy for increasing its critical current density. A TiO_2 additive was shown to form a second phase within a $\text{NZSP}(\text{TiO}_2)$ composite material, improving its Young's modulus and hardness, increasing its density, lowering interfacial resistance against Na metal, and increasing the adhesion between grains relative to polycrystalline NZSP synthesized in a similar way. The uniform distribution of TiO_2 at NZSP grain boundaries and on the surfaces modifies the NZSP microstructure without substantially impacting ionic or electronic conductivity, while also improving wettability of NZSP by metallic Na. A combination of XPS and

electrochemical measurements demonstrated that the above-mentioned effects synergistically interact to improve electrolyte performance. The TiO₂ additive in NZSP not only cuts the interfacial resistance in half and improves adhesion within the grain structure by more than a factor of 5, but also raises the critical current density at which Na dendrites form by an order of magnitude. These improvements can potentially enable a range of high-energy-density Na-ion batteries.

3. Experimental Section

Synthesis.

NZSP(TiO₂) composite pellets were prepared via a conventional solid-state reaction method. The starting stoichiometric precursors, Na₂CO₃ (99.99%, Aladdin), ZrO₂ (AR, Sinopharm), Anatase TiO₂ (average particle size, 40 nm) (99.8%, Aladdin), NH₄H₂PO₄ ($\geq 99.99\%$, Aladdin), SiO₂ (AR, Sinopharm), and isopropanol ($\geq 99.9\%$, Aladdin) were mixed by mechanical ball milling for 3 h. 10 wt% excess Na₂CO₃ was added to compensate for sodium volatilization during high-temperature heating (1150 °C). The mixture was subjected to a two-step sintering treatment. The mixed powder was then heated at 950 °C for 4 h, with a temperature ramp-up rate of 5 °C min⁻¹. The calcined powders were manually ground using a mortar and pestle, followed by further grinding in a planetary ball mill in isopropanol for 7 h, after which the material was held at 70 °C in a drying oven for 12 h. For every experiment, 0.3 g of processed powder was pressed uniaxially at about 7 MPa to form pellets with approximately 13 mm diameters and thicknesses of 0.9 ± 0.1 mm. Calcination of the cold-pressed pellets was performed at 1180 °C for 12 h, with a temperature ramp-up rate of 5 °C min⁻¹. Extra mother powders with the same composition were placed both underneath and on top of the pressed pellets in the Al₂O₃ crucible. To prepare NZSP and NZSP(TiO₂) samples with similar surface roughness for electrochemical measurements, the surfaces of the samples were first polished using SiC abrasive paper with 400 grits. The samples were sequentially polished by using successively finer SiC abrasives (1200 and 2500 grit). Ultimately, ultrasonic cleaning in isopropanol was performed to further ensure cleanliness of the pellets before experiments.

Characterization.

Mechanical properties. Mechanical properties of the NZSP(TiO₂) and NZSP samples were examined using a Nano Indenter (Hysitron TI-Premier Corp., Eden Prairie, MN) with a displacement resolution of 0.01 nm and a loading resolution of 50 nN. A cone-tip indenter was used. Different stress states were applied to the tip contact region to evaluate inherent strength of the samples. The applied force P increased at a constant loading rate up to the maximum force P_{\max} and then unloaded to zero at the same loading rate, 400 μNs^{-1} .

X-Ray Diffraction. X-ray diffraction (XRD) patterns of the as-prepared materials (powder and pellet) were obtained by using an X'pert Pro Powder Diffractometer (PANalytical) with Cu K α radiation in the range of $2\theta = 10\text{-}80^\circ$. Rietveld refinement was performed using GSAS software with the EXPGUI interface to determine the crystallographic data of NZSP(TiO₂) [42]. The surfaces and cross-sections of NZSP and NZSP(TiO₂) samples were characterized with a field-emission scanning electron microscope (FESEM, ZEISS Sigma 300, Germany). The morphology and crystal structures of NZSP and NZSP(TiO₂) samples were characterized by field emission transmission electron microscope and selected area electron diffraction (Tecnai G² F20 S-TWIN FEI with an accelerating voltage of 200 kV). The ToF-SIMS measurement was conducted using an ION-ToF (GmbH, Germany) ToF-SIMS 5 to detect the distribution of the TiO₂ phase on NZSP surfaces. The base pressure of the analysis chamber was $\sim 10^{-8}$ mbar. The action of the primary ion-beam bombardment on the sample surface induces an emission of negative secondary ions. Sputtering with a Cs⁺ ion beam (2 keV) was used for surface analysis, with sputtering areas of 20 \times 20, 100 \times 100, and 300 \times 300 μm^2 .

NZSP:TiO₂/Na interface XPS. The XPS system consists of several preparation chambers and an XPS/UPS analyzer (Phi 5000 Versa Probe) for analysis without breaking ultrahigh vacuum conditions [43, 44] (Figure S15). The base pressure of the experimental system was 5×10^{-9} mbar. The Na film was thermally evaporated stepwise out of a sodium dispenser (SAES Getters, Italy) in a separate chamber

accessible without breaking vacuum conditions. The deposition thickness of the metallic Na was controlled by applied current and deposition time. After one step Na deposition, the NZSP(TiO₂) sample was transferred to the XPS chamber through the tunnel with garage. After XPS measurement, the sample was transferred back to the Na dispenser chamber and then did the XPS measurement again. The process was repeated in this way till the Na 1s peak of metallic Na was detected. The carbonate molecules and pollutants absorbed on NZSP(TiO₂) surfaces were eliminated by heating NZSP(TiO₂) pellets at 450 °C under an O₂/Ar atmosphere. The characterization of the interface between Na and NZSP(TiO₂) was performed by stepwise Na deposition and near-surface XPS analysis. XPS tests were conducted using monochromatic Al-K α radiation (1486.6 eV) with a pass energy of 23.5 eV. The background of the core peaks was subtracted using the Shirley method. The peaks were fitted by using a pseudo-Voigt function^[45].

Contact Angle Measurements. The metallic Na block was melted in a stainless-steel crucible by heating it on a hot plate in a glovebox with an Ar atmosphere. The NZSP and NZSP(TiO₂) pellets were placed on a hot plate at 200 °C inside the glovebox to ensure that the sample temperature was higher than melting point of metallic Na (97 °C). Subsequently, molten Na was injected onto the pellet surface with a dropper. Photographs were also taken after Na-liquid drops were tipped off of the pellets.

Electrochemical performance of electrolyte/Na interface and solid-state battery assembly. NZSP pellets (Φ 12 mm diameter \times 0.8 mm thickness) were coated with Au by sputtering for impedance measurements with blocking electrodes. The Au film was coated on the surface of NZSP and NZSP(TiO₂) pellets by using a Sputter Coating System (*Quorum Q150R S UK*). The sputtering current was 50 mA and the sputtering time was 10 min. Impedance spectroscopy was conducted by using a Biologic multi-channel workstation between 1 Hz and 1 MHz with a signal amplitude of 10 mV. The electronic conductivity of NZSP was evaluated by DC polarization measurements between blocking electrodes. (Although Au forms an alloy with Na^[46], Au cations cannot readily enter the NZSP lattice, making the electrodes purely capacitive.) NZSP

pellets with Au coatings were prepared for the DC polarization measurements. A constant voltage (1 V) was held for 4000 seconds and the electronic conductivity was calculated from the steady-state current and the constant voltage by Ohm's law. Galvanostatic cycling experiments of Na/NZSP(TiO₂)/Na at a current density of 0.1 mA cm⁻² were performed by using a Landian battery tester (Wuhan, China). Critical current measurements were performed by the galvanostatic cycling at current densities stepping from 0.05-2 mA cm⁻² at 25 °C for Na/NZSP/Na and Na/NZSP(TiO₂)/Na cells with addition of tiny amount of liquid electrolyte (2 μL). The liquid electrolyte contained a composition of 1 M NaClO₄ in EC : DMC (1 : 1, by volume). The slurry was thoroughly mixed with NVP, super P and PVDF at a mass ratio of 80:10:10 in NMP (solvent, N-methyl-2-pyrrolidone). The slurry was coated on the surface of NZSP, and then, the Al foil was attached to the slurry-NZSP(TiO₂), placed into a vacuum oven and further dried overnight at 70 °C. The loading of the NVP cathode was 1.3 mg cm⁻². 5 μL high-voltage organic liquid electrolyte was added between the NVP cathode and NZSP(TiO₂) pellet to wet the cathode/NZSP(TiO₂) interface, which can avoid the influence of the cathode/NZSP(TiO₂) resistance on the battery performances. All the assembled cells were tested at 25 °C by using a Neware battery tester (China). The cut voltages were set at 2.0-3.8 V with different current densities (NVP, 1C = 117 mAh g⁻¹).

Supporting Information

Supporting Information is available from the Wiley Online Library or from the author.

Acknowledgments

This work was supported by the National Natural Science Foundation of China (Nos. 51632001 and U1764256). CWM and GL were supported by the EPSRC Faraday Institution SOLBAT project, subaward FIRG007 under grant EP/P003532/1.

Author Contributions

All authors have given approval to the final version of the manuscript.

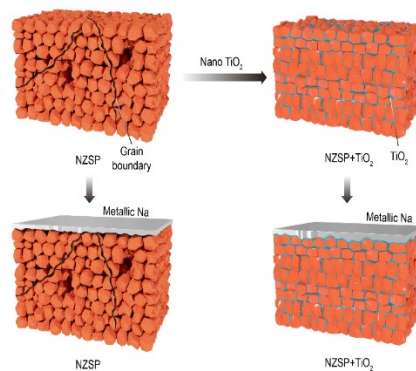
Notes

The authors declare that they have no competing interests.

ToC: TiO₂ is incorporated into NZSP as a second phase, which can improve density, make grains more adherent, reduce microscopic defects, and lower the interfacial resistance against metallic Na, thereby raising the critical current density.

Zhonghui Gao, Jiayi Yang, Guanchen Li, Thimo Ferber, Junrun, Feng, Yuyu, Li, Haoyu Fu, Wolfram Jaegermann, Charles W. Monroe, Yunhui Huang*

TiO₂ as second phase in Na₃Zr₂Si₂PO₁₂ to suppress dendrite growth in sodium metal solid-state batteries



References

- [1] T. Famprikis, P. Canepa, J. A. Dawson, M. S. Islam, C. Masquelier, *Nat. Mater.* **2019**, *18*, 1278-1291.
- [2] C. Zhao, L. Liu, X. Qi, Y. Lu, F. Wu, J. Zhao, Y. Yu, Y.-S. Hu, L. Chen, *Adv. Energy Mater.* **2018**, *8*, 1703012.
- [3] Z. Gao, H. Sun, L. Fu, F. Ye, Y. Zhang, W. Luo, Y. Huang, *Adv. Mater.* **2018**, *30*, 1705702.
- [4] M. Guin, F. Tietz, *J. Power Sources* **2015**, *273*, 1056-1064.
- [5] Z. Z. Zhang, Z. Y. Zou, K. Kaup, R. J. Xiao, S. Q. Shi, M. Avdeev, Y. S. Hu, D. Wang, B. He, H. Li, X. J. Huang, L. F. Nazar, L. Q. Chen, *Adv. Energy Mater.*

- 2019**, 1902373.
- [6] Z. Z. Zhang, Q. H. Zhang, J. N. Shi, Y. S. Chu, X. Q. Yu, K. Q. Xu, M. Y. Ge, H. F. Yan, W. J. Li, L. Gu, Y. S. Hu, H. Li, X. Q. Yang, L. Q. Chen, X. J. Huang, *Adv. Energy Mater.* **2016**, 1601196.
- [7] E. J. Cheng, A. Sharafi, J. Sakamoto, *Electrochim. Acta* **2017**, 223, 85-91.
- [8] X. Ji, S. Hou, P. Wang, X. He, N. Piao, J. Chen, X. Fan, C. Wang, *Adv. Mater.* **2020**, 32, 2002741.
- [9] H. Koshikawa, S. Matsuda, K. Kamiya, M. Miyayama, Y. Kubo, K. Uosaki, K. Hashimoto, S. Nakanishi, *J. Power Sources* **2018**, 376, 147-151.
- [10] R. Hongahally Basappa, T. Ito, T. Morimura, R. Bekarevich, K. Mitsuishi, H. Yamada, *J. Power Sources* **2017**, 363, 145-152.
- [11] L. Cheng, W. Chen, M. Kunz, K. Persson, N. Tamura, G. Chen, M. Doeff, *ACS Appl. Mater. Interfaces* **2015**, 7, 2073-81.
- [12] C. Monroe, J. Newman, *J. Electrochem. Soc.* **2005**, 152, 396-404.
- [13] S. Yu, D. J. Siegel, *ACS Appl. Mater. Interfaces* **2018**, 10, 38151-38158.
- [14] M. Klinsmann, F. E. Hildebrand, M. Ganser, R. M. McMeeking, *J. Power Sources* **2019**, 442.
- [15] L. Porz, T. Swamy, B. W. Sheldon, D. Rettenwander, T. Frömling, H. L. Thaman, S. Berendts, R. Uecker, W. C. Carter, Y.-M. Chiang, *Adv. Energy Mater.* **2017**, 7, 1701003.
- [16] F. Han, A. S. Westover, J. Yue, X. Fan, F. Wang, M. Chi, D. N. Leonard, N. J. Dudney, H. Wang, C. Wang, *Nat. Energy* **2019**, 4, 187-196.
- [17] T. Krauskopf, H. Hartmann, W. G. Zeier, J. Janek, *ACS Appl. Mater. Interfaces* **2019**, 11, 14463-14477.
- [18] J. Kasemchainan, S. Zekoll, D. Spencer Jolly, Z. Ning, G. O. Hartley, J. Marrow, P. G. Bruce, *Nat. Mater.* **2019**, 18, 1105-1111.
- [19] R. H. Basappa, T. Ito, H. Yamada, *J. Electrochem. Soc.* **2017**, 164, 666-671.
- [20] T. Swamy, R. Park, B. W. Sheldon, D. Rettenwander, L. Porz, S. Berendts, R. Uecker, W. C. Carter, Y.-M. Chiang, *J. Electrochem. Soc.* **2018**, 165,

3648-3655.

- [21] W. Manalastas, J. Rikarte, R. J. Chater, R. Brugge, A. Aguadero, L. Buannic, A. Llordés, F. Aguesse, J. Kilner, *J. Power Sources* **2019**, *412*, 287-293.
- [22] H. Tang, Z. Deng, Z. Lin, Z. Wang, I.-H. Chu, C. Chen, Z. Zhu, C. Zheng, S. P. Ong, *Chem. Mater.* **2017**, *30*, 163-173.
- [23] S. Wang, H. Xu, W. Li, A. Dolocan, A. Manthiram, *J. Am. Chem. Soc.* **2018**, *140*, 250-257.
- [24] X. Han, Y. Gong, K. K. Fu, X. He, G. T. Hitz, J. Dai, A. Pearse, B. Liu, H. Wang, G. Rubloff, Y. Mo, V. Thangadurai, E. D. Wachsman, L. Hu, *Nat. Mater.* **2017**, *16*, 572-579.
- [25] J. Yang, Z. Gao, T. Ferber, H. Zhang, C. Guhl, L. Yang, Y. Li, Z. Deng, P. Liu, C. Cheng, R. Che, W. Jaegermann, RenéHausbrand, Y. Huang, *J. Mater. Chem. A* **2020**, *8*, 7828-7835.
- [26] A. Kato, A. Hayashi, M. Tatsumisago, *J. Power Sources* **2016**, *309*, 27-32.
- [27] Kun (Kelvin) Fu, Yunhui Gong, Boyang Liu, Yizhou Zhu, Shaomao Xu, Yonggang Yao, Wei Luo, Chengwei Wang, Steven D. Lacey, Jiaqi Dai, Yanan Chen, Yifei Mo, Eric Wachsman, L. Hu, *Sci. Adv.* **2017**, *3*, 1601659.
- [28] W. Luo, Y. Gong, Y. Zhu, K. K. Fu, J. Dai, S. D. Lacey, C. Wang, B. Liu, X. Han, Y. Mo, E. D. Wachsman, L. Hu, *J. Am. Chem. Soc.* **2016**, *138*, 12258-62.
- [29] W. Luo, Y. Gong, Y. Zhu, Y. Li, Y. Yao, Y. Zhang, K. K. Fu, G. Pastel, C. F. Lin, Y. Mo, E. D. Wachsman, L. Hu, *Adv. Mater.* **2017**, *29*, 1606042.
- [30] P. Bai, J. Guo, M. Wang, A. Kushima, L. Su, J. Li, F. R. Brushett, M. Z. Bazant, *Joule* **2018**, *2*, 2434-2449.
- [31] A. S. Westover, R. L. Sacci, N. Dudney, *ACS Energy Lett.* **2020**, *5*, 3860-3867.
- [32] R. Choudhury, M. Wang, J. Sakamoto, *J. Electrochem. Soc.* **2020**, *167*, 140501.
- [33] P. Hartmann, T. Leichtweiss, M. R. Busche, M. Schneider, M. Reich, J. Sann, P. Adelhelm, J. Janek, *J. Phys. Chem. C* **2013**, *117*, 21064-21074.
- [34] J. A. Lewis, J. Tippens, F. J. Q. Cortes, M. T. McDowell, *Trends in Chemistry*

- 2019**, *1*, 845-857.
- [35] A. Sharafi, C. G. Haslam, R. D. Kerns, J. Wolfenstine, J. Sakamoto, *J. Mater. Chem. A* **2017**, *5*, 21491-21504.
- [36] X. G. Cao, X. H. Zhang, T. Tao, H. Y. Zhang, *Ceram. Int.* **2020**, *46*, 8405-8412.
- [37] D. Chen, F. Luo, L. Gao, W. Zhou, D. Zhu, *J. Electron. Mater.* **2017**, *46*, 6367-6372.
- [38] H. Guo, J. Su, W. Zha, T. Xiu, Z. Song, M. E. Badding, J. Jin, Z. Wen, *J. Alloys Compd.* **2021**, *856*, 157222.
- [39] J.-N. Zhang, Q. Li, C. Ouyang, X. Yu, M. Ge, X. Huang, E. Hu, C. Ma, S. Li, R. Xiao, W. Yang, Y. Chu, Y. Liu, H. Yu, X.-Q. Yang, X. Huang, L. Chen, H. Li, *Nat. Energy* **2019**, *4*, 594-603.
- [40] G. Li, C. W. Monroe, *Phys. Chem. Chem. Phys.* **2019**, *21*, 20354-20359.
- [41] A. Sharafi, E. Kazyak, A. L. Davis, S. Yu, T. Thompson, D. J. Siegel, N. P. Dasgupta, J. Sakamoto, *Chem. Mater.* **2017**, *29*, 7961-7968.
- [42] B. Toby, *J. Appl. Crystallogr.*, **2001**, *34*, 210.
- [43] C. Guhl, M. Fingerle, R. Hausbrand, *J. Power Sources* **2017**, *362*, 299-307.
- [44] Z. Gao, J. Yang, H. Yuan, H. Fu, Y. Li, Y. Li, T. Ferber, C. Guhl, H. Sun, W. Jaegermann, R. Hausbrand, Y. Huang, *Chem. Mater.* **2020**, *32*, 3970-3979.
- [45] D. A. Shirley, *Phys. Rev. B* **1972**, *5*, 4709-4714.
- [46] A. Sommer, *Nature* **1943**, *152*, 215.